Facet-Dependent Electrical Conductivity Properties of PbS Nanocrystals

Chih-Shan Tan‡, **Hsiang-Sheng Chen**†, **Chun-Ya Chiu**†, **Szu-Chieh Wu**†, **Lih-Juann Chen**‡, and **Michael H. Huang***†

†Department of Chemistry and ‡Department of Materials Science and Engineering, National Tsing Hua University, Hsinchu 30013, Taiwan

DOI: 10.1021/acs.chemmater.6b00274

Publication Date (Web): February 11, 2016

*E-mail: hyhuang@mx.nthu.edu.tw.

Abstract

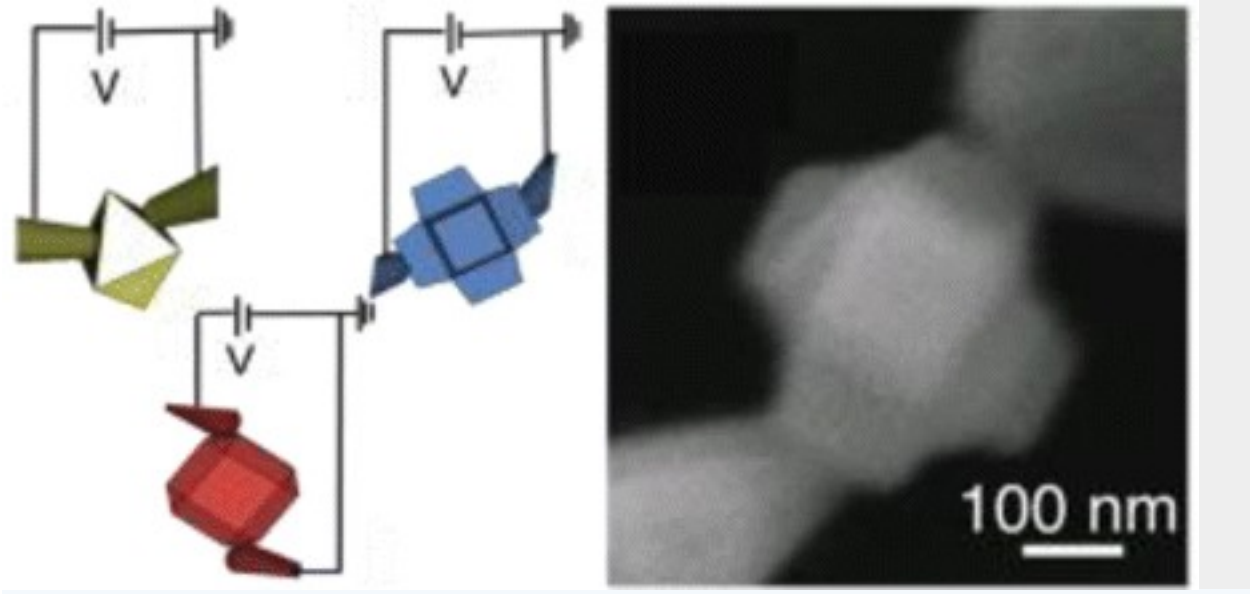

Large PbS protruded cubes, edge- and corner-truncated cubes and octahedra, and perfect octahedra with sizes over 200 nm have been synthesized in aqueous solution. By using two surface oxide-free tungsten probes to contact a clean particle, these PbS nanocrystals displayed facet-dependent electrical conductivity behaviors. Both {110} and {100} faces are highly conductive at applied voltages beyond 4 V, but the {111} faces can remain nonconductive even at 5 V. An asymmetric *I*–*V* curve was recorded when electrical contacts were made simultaneously on the {110} and {111} facets of a truncated cube. A modified band diagram of PbS is constructed to account for the observed facet-dependent effect. Density of states plots for varying numbers of PbS surface planes show larger areas of conduction band electron occupancy for the (110) and (100) planes than that for the (111) planes at a layer thickness of 3.0–3.4 nm. The work represents that, for the first time, the facet-dependent electrical properties of an n-type semiconductor nanocrystal

are directly probed. Facet-dependent electrical conductivity should be a general semiconductor property and can be exploited to fabricate single-nanocrystal operating electronic components.

Introduction

Synthesis of polyhedral semiconductor nanocrystals with sharp faces and a variety of particle morphologies should be quite useful for the examination of their various facet-dependent properties. (1) Previously, photocatalytic activity,(2-4) electrical conductivity,(5, 6) and even optical properties of Cu_2O crystals have been shown to be strongly facet-dependent by using primarily cubes, octahedra, and rhombic dodecahedra exposing, respectively, {100}, {111}, and {110} surfaces for such investigations.(7-11) Facet-dependent optical properties of Cu_2O nanocrystals were demonstrated by taking UV–vis absorption spectra of Au–Cu_2O and Pd–Cu_2O core–shell nanocrystals with different particle shapes and tunable sizes. Using two surface oxide-free tungsten probes to make contacts to a single Cu_2O cube, octahedron, and rhombic dodecahedron, strongly facet-dependent electrical conductivity behaviors of Cu_2O were revealed. A Cu_2O octahedron is highly electrically conductive, while a cube is not conductive below an applied voltage of 3 V. On the other hand, a rhombic dodecahedron is completely nonconductive even at 5 V. An asymmetric *I*–*V* curve resembling that seen for a p–n junction was obtained with tungsten probes contacting two different facets of a Cu_2O crystal. This effect is explained in terms of the presence of a thin surface layer with different band structures and degrees of band bending for different surface facets of a crystal and thus is applicable to other semiconductors.(6) It is highly interesting to examine possible facet-dependent electrical conductivity properties of other semiconductor materials. PbS nanocrystals with various polyhedral morphologies and sizes of less than 100 nm can be synthesized using a number of synthetic approaches.(12-18) However, growth of sufficiently large PbS crystals with sizes over 200 nm is necessary for electrical conductivity measurements on a single particle, because the tungsten probe tips cannot be fabricated so consistently sharp for precise facet contact. Previously, we have developed a one-pot synthesis method to grow PbS nanocubes and octahedra in aqueous solution. (18, 19) By changing the reagent introduction sequence, large truncated PbS octahedra with sizes over 200 nm have been obtained.(19) Facet-dependent dispersions of PbS nanocrystals in negatively charged methyl orange and positively charged methylene blue solutions have been observed.(19)

In the present study, we have modified the reaction conditions to directly grow large PbS edge- and corner-truncated cubes, face-protruded cubes, octahedra, and edge- and corner-truncated octahedra with sizes above 200 nm. The particles possess sharp faces well suited for facet-dependent electrical conductivity measurements. *I*–*V* curves for the three low-index facets have been recorded, showing again a large facet-dependent effect. An asymmetric *I*–*V* curve was obtained when the probes contact simultaneously a conductive face and a nonconductive face on a single PbS crystal. DOS calculations on different layers of PbS planes have been performed. DOS plots show conduction band area differences for the (100), (110), and (111) planes at thicknesses of 3.0–3.4 nm from the surface, which roughly match with their electrical conductivity responses. This example further demonstrates that facet-dependent electrical response is a general property for semiconductor nanocrystals.

Experimental Section

Synthesis of Large PbS Nanocrystals

Face-raised or protruded PbS cubes and edge- and corner-truncated cubes were synthesized following a similar procedure. First, 0.01 g of cetyltrimethylammonium bromide (CTAB, 98%, Alfa Aesar) was added to a 25 mL vial, followed by the addition of 6.3 mL of deionized water, 0.5 mL of 1.0 M nitric acid solution (HNO_3, 65%, Fluka), 3.0 mL of thioacetamide solution (TAA, 99%, Sigma-Aldrich), and 0.2 mL of lead acetate solution ($Pb(CH_3COO)_2$, 99%, Alfa Aesar). The total solution volume is 10 mL. The vial was placed in an oven heated to 90 °C for 3 h in the production of face-raised cubes. By extending the reaction time to 12 h, exclusive edge- and corner-truncated cubes were obtained. The product was cooled to room temperature using a cold water bath, followed by centrifugation at 5000 rpm for 7 min. After careful removal of the top transparent solution, leaving the dark precipitate behind, 10 mL of deionized water was added, and the solution was centrifuged again at 5000 rpm for 7 min. The same washing procedure was repeated two more times to fully remove CTAB.

PbS octahedra and edge- and corner-truncated octahedra were synthesized using a similar reaction condition. First, 0.01 g of CTAB was added to a 25 mL vial, followed by the introduction of 0.05 mL of 0.1 M lead acetate solution and 0.05 mL of 1.0 M nitric acid solution. To prepare PbS octahedra, 0.2 mL of 0.1 M TAA solution and 9.7 mL of deionized water were added. To make edge- and corner-truncated octahedra, 1.5 mL of 0.1 M TAA solution and 8.4 mL of deionized water were introduced. Total solution volume is 10 mL in both cases. After 2 h of reaction at 90 °C in an oven,

the product was cooled to room temperature using a cold water bath, followed by centrifugation at 5000 rpm for 7 min. The same particle washing procedure as above was used.

Instrumentation and DOS Calculations

SEM images of the samples were obtained using a JEOL JSM-7000F electron microscope. TEM characterization was performed on a JEOL JEM-2100 electron microscope with an operating voltage of 200 kV. XRD patterns were recorded on a Shimadzu XRD-6000 diffractometer with Cu Kα radiation. A Keithley 2400 source meter was used for electrical measurements. Hall effect measurements were carried out on an Ecopia HMS-3000 instrument. X-ray photoelectron spectroscopy (XPS) spectra were obtained using a ULVAC-PHI Quantera SXM high-resolution XPS spectrometer. Data were recorded with a monochromatized Al anode as the excitation source. The C 1s peak was used as the reference peak.

The model of PbS is constructed by combining a 5 × 5 × 5 supercell of the PbS structure and selecting the specific facet to slice. Geometry optimization caluclations were performed by density function theory (DFT) to establish structures of different facets of PbS with different thicknesses. First-principles calculations were based on DFT(20) with the Perdew–Burke–Ernzerhof generalized gradient approximation (PBE-GGA)(21) with a *k*-point mesh as 7 × 7 × 1 and 0.1 eV broadening value. Fly pseudopotentials with no dipole correction were used. The plane-wave basis set cutoff is 500 eV. The Cambridge Serial Total Energy Package (CASTEP) was used to calculate the density of states (DOS) of PbS facet structures.

Results and Discussion

In this study, PbS nanocrystals were synthesized in an aqueous solution containing lead acetate, thioacetamide, CTAB surfactant, and nitric acid. TAA serves as the sulfide source. The following reactions should occur to form PbS particles.

$$Pb^{2+} + CH_3C(S)NH_2 + H_2O \rightarrow PbS + CH_3C(O)NH_2 + 2H^+ \quad (1)$$

$$S^{2-} + 2H^+ \rightarrow H_2S \quad (2)$$

Because PbS is formed by a precipitation reaction, addition of nitric acid can lower the equilibrium constant for eq 1 toward the forward reaction forming PbS precipitate. PbS may be formed more slowly to yield nanocrystals with shape control. Such a strategy has been adopted for the growth of Ag_2O crystals with systematic shape evolution.(22-25) Figure 1 shows SEM and TEM characterization of the synthesized PbS nanocrystals. PbS face-raised cubes and edge- and corner-truncated cubes were synthesized by adding a lesser amount of lead acetate, a larger amount of TAA, and 10 times more nitric acid than those used in the formation of PbS octahedra and truncated

octahedra. These reaction conditions were formulated recognizing that relative Pb^{2+} and S^{2-} concentrations and control of particle growth rate can tune the particle shape. The particles are highly uniform in shape and mostly 200–300 nm in size for cubes and 300–400 nm for octahedra. TEM analysis confirmed that the protruded faces are the {100} faces. The edge- and corner-truncated cubes and octahedra possess {100}, {111}, and {110} faces. Octahedra are bound by entirely {111} faces. The split diffraction spots seen in the selected-area electron diffraction (SAED) pattern of an edge- and corner-truncated octahedron are likely due to the shape effect relating to its special morphology, since there is no second phase present, as evidenced by XRD analysis (see Figure S1). Because of their preferential orientation of deposition on the substrate, XRD spectra for PbS octahedra and edge- and corner-truncated cubes give predominantly (111) and (200) peaks, respectively. For the other particle shapes, the nanocrystals may be more randomly oriented such that other reflection peaks are also observed. The (111) peak remains strongest for the truncated octahedra and protruded cubes. The clean nanocrystals were subsequently used for electrical conductivity measurements.

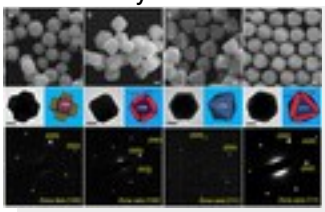

Figure 1. SEM images, TEM images, and SAED patterns of the synthesized PbS: (a) protruded cubes, (b) edge- and corner-truncated cubes, (c) octahedra, and (d) edge- and corner-truncated octahedra. All scale bars are equal to 100 nm.

XPS data on the washed PbS octahedra and edge- and corner-truncated cubes indicate that the nanocrystals are surfactant-free after the washing procedure (see Figure S2). Previously, XPS spectra were also used to confirm the complete removal of surfactant after the washing steps in the synthesis of Pd nanocrystals.(26) A drop of surfactant-free PbS particle solution was added to a clean Si (111) wafer previously annealed in an air atmosphere at 900 °C for 48 h to form a 500 nm thick silicon oxide film. The oxide layer serves as an insulator to prevent current leakage through the underlying substrate. Once the substrate was loaded into an SEM microscope equipped with a nanomanipulator, two tungsten probes fabricated electrochemically were brought into contact with their tips. A sweep voltage from 0 to 5 V with a current limit of 1 μA was applied to remove surface oxide by Joule heating. Initially, the *I*–*V* curves for the contacted probes showed a retarded behavior due to a native oxide layer on the probe surface. The sweeping voltage was applied until a linear *I*–*V* curve was achieved, signifying removal of surface oxide, and the resistance was ∼20 Ω. After that,

the probes were moved to contact a single particle for conductivity measurements (see Figure S3). Several measurements were made until the probes become loose due to small shock from the current. Current is normally highest for the first couple of measurements.

Figure 2 shows SEM images of two tungsten probes touching the {110} edges of a PbS truncated cube (tip-to-tip distance of 327 nm), {100} faces of a protruded cube (tip-to-tip distance of 300 nm), {111} faces of an octahedron (tip-to-tip distance of 300 nm), and the measured *I*–*V* curves. The particle sizes are similar in terms of probe tip separation. At high voltages, the {110} facets can give appreciably higher currents than the {100} facets. At 5 V, the current passing through the {110} faces reaches 4000 nA, while for the {100} case, it is about 3500 nA. In contrast, the {111} facets are almost nonconductive and the current can only reach to 80 nA at 5 V. The currents across the {110} and {100} facets are 50 and 43.8 times higher than that for the {111} facets, respectively. Clear facet-dependent electrical conductivity behaviors have been observed in PbS nanocrystals. Figure S4 provides additional *I*–*V* curves with tungsten probes contacting the same particles shown in Figure 2. Here, electrical conductivity for the {100} and {110} facets appear similar. Please note that, even for the most conductive {110} facets, current does not rise as quickly as that seen for the conductive {111} facets of Cu_2O. There is an obvious lag in rising current with applied voltage, which is characteristic of semiconductor *I*–*V* response. Interestingly, the least conductive PbS facet is the {111} face, while this face is most conductive in Cu_2O. Thus, the relative facet conductivity trend is different for different materials. Again, please note that the recorded *I*–*V* curves are not exactly symmetrical because the probe contact areas are different due to tip size variation.

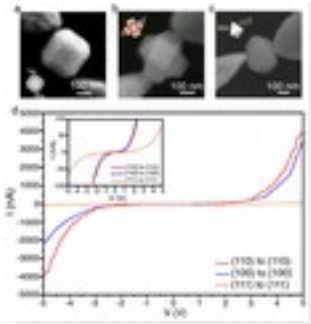

Figure 2. (a) SEM images of an edge- and corner-truncated PbS cube with tungsten probes contacting its {110} faces. (b) SEM image of a protruded PbS cube with tungsten probes contacting its {100} faces. (c) SEM image of a PbS octahedron with tungsten probes contacting its {111} faces. Schematic illustrations are provided for the three cases. (d) The measured *I*–*V* curves. Inset shows the expanded *I*–*V*curves.

Since different particles such as truncated cubes and octahedra with different sizes but exposing the same facets have been synthesized, more conductivity measurements have been performed to evaluate the effects of particle size on the magnitude of current generated. Figure S5 offers *I*–

*V*curves with tungsten probes making contacts to the {110} faces of a truncated PbS cube and a truncated octahedron. The smaller octahedron (300 nm) is obviously more conductive with the current reaching 5500 nA at 5 V than the bigger cube (327 nm) having a maximum current of 4000 nA at 5 V. It is reasonable that smaller particles should generally deliver higher currents because of shorter carrier transport distances. However, when the opposite {100} faces of a face-raised PbS cube (300 nm) and an edge- and corner-truncated cube (240 nm) were contacted for electrical measurements, the 240 nm cube shows similar current as that of the 300 nm cube (Figure S6). Presumably, the size effect is less important as particles get smaller. The same comparison was performed on the {111} facets. Here, tungsten probes contacted opposite, but not parallel, {111} faces of a PbS octahedron in one case with a probe tip-to-tip distance of 300 nm. In another case, opposite and parallel {111} faces of an octahedron were contacted on another particle with a tip-to-tip distance of 240 nm (Figure S7). Here, the 300 nm octahedron showed better conductivity with current reaching ~75 nA at 5 V. The 240 nm octahedron is essentially nonconductive with a current of only 9 nA at 5 V. A typical opposite {111} face contact gives the lowest current. The data suggest that locations of electrical contact may be important. Comparing the highest {110} current to the lowest {111} current recorded, the difference can reach beyond 610 times, showing its potential as single-particle electronic switches.

The facet-dependent electrical conductivity properties of PbS can be understood by presenting its modified band diagram. Before constructing the band diagram, Hall effect measurements on a film of smaller PbS nanocubes synthesized using our previously reported procedure were conducted to determine the type of current carrier.(19) The PbS nanocubes were found to be n-type semiconductors with a negative value for bulk carrier concentration (data not shown). Please note that contact failure resulting in unsuccessful measurements can easily happen even after washing of the particles to completely remove surfactant before depositing a 2–3 μm thick film, suggesting that multiple interparticle contacts can lead to loss of conductivity. Figure 3 is the modified band diagram of PbS in contact with tungsten metal. The valence and conduction bands are drawn to bend down at the interface because W has a relatively small work function at 4.55 eV and the particles were measured to be n-type semiconductors.(27-29) The degrees of interfacial band bending are drawn to reflect the observed electrical conductivity differences for the three facets of PbS (i.e., {110} ≥ {100} ≫ {111}). The {111} band edge is drawn most deviated from the bulk energy levels, showing that the {111} face has the highest barrier for electrons to move pass through this surface from tungsten. The degrees of {110} and {100} band bending are closer, but the {110} facet presents less bending and a lower barrier height.

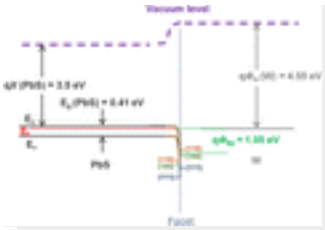

Figure 3. Modified band diagram of PbS with consideration of relative band edge energies of different crystal surfaces. In the diagram, qX is semiconductor electron affinity, $q\Phi_s$ is semiconductor work function, $q\Phi_m$ is metal work function, $q\Phi_{Bp}$ is energy barrier of the W and PbS contact, E_c is conduction band energy, E_v is valence band energy, and E_f is Fermi level. Valence band energies for the various surfaces are shown to the left of the blue facet line, while conduction band energies are marked to the right side of the line.

Previous studies on sub-10 nm PbS quantum dots have shown that their electronic properties can be altered from pristine semiconducting behavior to metallic behavior by modifying the particle surfaces with capping ligands.(30-33) This surface modification can cause Pb/S stoichiometric tuning and the formation of midgap surface states, thereby improving the electrical conductivity of the particles. We believe such surface compositional variation is most effective for quantum dots with a large surface-to-volume ratio. In the present study, XPS spectra indicate that the CTAB surfactant has been cleanly removed from the surfaces of the synthesized PbS cubes and octahedra after the washing process. Furthermore, positions of the Pb 4f peaks at 137.0 and 141.9 eV and S 2p peaks at 160.4 and 161.6 eV for octahedra and edge- and corner-truncated cubes are identical, showing that their surface chemical bonding states are the same. Since no capping agent was intentionally introduced, the surface chemical environment should be the same for the {100}, {111}, and {110} faces of the PbS nanocrystals. There is no experimental evidence to suggest the presence of any surface stoichiometric alteration and the formation of midgap states in these crystals. The observed large electrical conductivity differences should be explained in terms of facet effects.

It is also interesting to obtain *I*–*V* curves with probes contacting simultaneously a conductive facet and a nonconductive facet of a single PbS particle. Figure 4 shows an SEM image of tungsten probes touching the {111} and {110} facets of an edge- and corner-truncated PbS cube. An asymmetric *I*–*V* curve was generated. An *I*–*V* response similar to that for a p–n junction is possible using a single PbS nanocrystal, if the voltage sweeping range is from −2.5 to +5 V. Here, the positive voltage portion corresponds to the forward bias domain in the *I*–*V* curve of a p–n junction, where electrical current flows into the crystal through the {110} face and exiting the crystal from the {111} face. In the negative voltage portion corresponding to the reverse bias domain in the *I*–*V* curve of a p–n junction, current flows into the crystal through the {111} face and exits from the {110} face. It

is unclear why fairly high current was still recorded at −5 V, but better and exclusive {111} face contact should extend the zero-current portion to more negative voltages. Figure 5gives another modified band diagram of a PbS crystal specific for this electrical contact case. If current flows into the crystal through the {110} face, it sees a lower barrier, and electrons move easily into the crystal under sufficiently high applied voltages. Current exiting the crystal meets the {111} face with a much higher barrier, but electron accumulation in the conduction band should raise their energy level for facile current flow over the {111} barrier. On the other hand, when current flows to the {111} face, it sees a much greater barrier, so a lower current was recorded. Once electrons move past the barrier into the crystal, exiting from the {110} faces is not a problem. However, that the fact current flowing into the crystal is more difficult means that ultimately this direction of current flow leads to low conductivity. Thus, a rectifying effect has been created with the potential to function as a field-effect transistor. Similar to that found in Cu_2O crystals, a PbS single particle can also function as an operating electronic component turning current on or off by simply changing the applied voltage or current flow direction through a crystal.

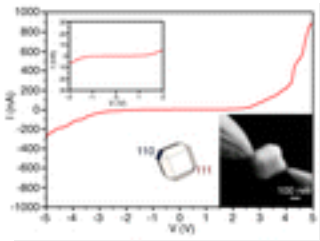

Figure 4. SEM image showing two tungsten probes making contacts to the {111} and {110} facets of an edge- and corner-truncated PbS cube and the measured *I*–*V* curve. Inset shows the expanded *I*–*V* curves. Schematic drawing of the contacted facets is also provided.

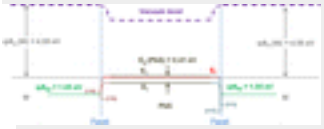

Figure 5. Modified band diagram of a PbS crystal with its {111} and {110} facets in contact with tungsten probes. This figure highlights the relative heights of energy barriers encountered when electrical current flows from the {111} side or the {110} side of the crystal into the crystal interior. The energy barrier is much smaller when current flows into the crystal from the {110} face.

The existence of facet-dependent electrical, photocatalytic, and optical properties can be explained in terms of the presence of a thin surface layer on a semiconductor crystal with different degrees of band bending and band structures for different facets.(1) DOS calculations have been performed to generate DOS plots for the three facets with varying numbers of lattice planes counting from the

surface. Figures S8–S10 provide the DOS plots. Unlike the DOS plots for Cu_2O, the initially continuous energy levels open up several gaps below the Fermi level as the number of plane increases. Since conducting electrons should have energies above this level (the 0 eV line), we have focused on features in the positive eV region to explain the observed conductivity differences. We determined that a layer thickness of 3.0–3.4 nm is a reasonable thickness to compare the DOS plots for these surface planes. Figure 6 shows the DOS plots for the (100) planes with a 5-layer thickness (3.0 nm), (110) planes with an 8-layer thickness (3.4 nm), and (111) planes with a 10-layer thickness (3.4 nm). A tiny gap above the Fermi level seems to be present for all three facets in this thickness range. When comparing the area of electron density of states above the Fermi level within this chosen layer thickness, the (100), (110), and (111) planes yield values of approximately 712, 582, and 516 in electron occupancy for the conduction band. The data show that different facets around the same thickness (3 nm) should originally have different amounts of electrons in the conduction band. Significant larger values for the (100) and (110) planes may mean more electrons occupying the high energy levels (conduction levels) at these facets, which is related to their better electrical conductivity. In this respect, the DOS results roughly match the experimentally observed conductivity trend. The results also indicate that the surface layer responsible for the facet-dependent effects in PbS is much thicker at 3 nm than that for Cu_2O at ~1 nm or less.

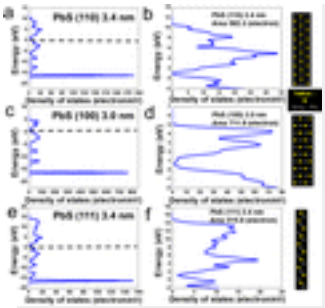

Figure 6. Density of states plots for the (a, b) (100), (c, d) (110), and (e, f) (111) planes of PbS consisting of 5, 8, and 10 layers of these planes. Models for three layers of lattice planes are shown. The conduction band of (100) planes is from 1 to 5 eV, the conduction band of (110) planes is from 1 to 11 eV, and the conduction band of (111) planes is from 1 to 15 eV.

Conclusion

Large PbS protruded cubes, octahedra, truncated cubes, and truncated octahedra with sizes above 200 nm have been synthesized directly in aqueous solution. The clean particles were found to exhibit facet-dependent electrical conductivity behaviors. The {110} and {100} faces are highly

conductive beyond 4 V, while the {111} facets can remain nonconductive even at 5 V. An asymmetric *I*–*V* curve was recorded when electrical circuit was made through the {110} and {111} facets of a single particle. DOS plots show that the (110) and (100) surface planes may accommodate more conducting electrons than the (111) surface planes. The thin surface layer responsible for the facet-dependent electrical behaviors may have a thickness of ∼3 nm. This work demonstrates that both p-type (for Cu_2O) and n-type semiconductors possess facet-dependent electrical conductivity properties for integration of single nanocrystals in functional electronic devices.

Supporting Information

The Supporting Information is available free of charge on the ACS Publications website at DOI: 10.1021/acs.chemmater.6b00274.

- XRD spectra of the synthesized PbS crystals, additional *I*–*V* curves, and DOS plots for the (100), (110), and (111) planes of PbS consisting of different plane layers (PDF)

- **PDF**
  - cm6b00274_si_001.pdf (3.33 MB)

Facet-Dependent Electrical Conductivity Properties of PbS Nanocrystals

figshare

ShareDownload

The authors declare no competing financial interest.

Acknowledgment

We thank the Ministry of Science and Technology of Taiwan for the support of this research (NSC 101-2628-M-007-006 and MOST 102-2633-M-007-002). We thank Dr. Yu-Jung Lu in the Department of Physics at National Tsing Hua University for assistance in the Hall effect measurements. We greatly appreciate the use of the facility at the Center for Nanotechnology, Materials Science, and Microsystems of National Tsing Hua University.

- Reference QuickView
-

References

This article references 33 other publications.

1. 1.

   Huang, M. H.; Rej, S.; Hsu, S.-C. Facet-Dependent Properties of Polyhedral Nanocrystals *Chem. Commun.***2014**, 50, 1634– 1644 DOI: 10.1039/c3cc48527g

   [Crossref], [PubMed], [CAS]

2. 2.

   Wang, W.-C.; Lyu, L.-M.; Huang, M. H. Investigation of the Effects of Polyhedral Gold Nanocrystal Morphology and Facets on the Formation of Au–Cu_2O Core–Shell Heterostructures *Chem. Mater.* **2011**, 23,2677– 2684 DOI: 10.1021/cm200708q

   [ACS Full Text], [CAS]

3. 3.

   Huang, W.-C.; Lyu, L.-M.; Yang, Y.-C.; Huang, M. H. Synthesis of Cu_2O Nanocrystals from Cubic to Rhombic Dodecahedral Structures and Their Comparative Photocatalytic Activity *J. Am. Chem. Soc.* **2012**,134, 1261– 1267 DOI: 10.1021/ja209662v

   [ACS Full Text], [CAS]

4. 4.

   Zhang, Y.; Deng, B.; Zhang, T.; Gao, D.; Xu, A.-W. Shape Effects of Cu_2O Polyhedral Microcrystals on Photocatalytic Activity *J. Phys. Chem. C* **2010**, 114, 5073– 5079 DOI: 10.1021/jp9110037

   [ACS Full Text], [CAS]

5. 5.

   Kuo, C.-H.; Yang, Y.-C.; Gwo, S.; Huang, M. H. Facet-Dependent and Au Nanocrystal-Enhanced Electrical and Photocatalytic Properties of Au–Cu_2O Core–Shell Heterostructures *J. Am. Chem. Soc.* **2011**, 133,1052– 1057 DOI: 10.1021/ja109182y

   [ACS Full Text], [CAS]

6. 6.

Tan, C.-S.; Hsu, S.-C.; Ke, W.-H.; Chen, L.-J.; Huang, M. H. Facet-Dependent Electrical Conductivity Properties of Cu_2O Crystals *Nano Lett.* **2015**, 15, 2155– 2160 DOI: 10.1021/acs.nanolett.5b00150

[ACS Full Text], [CAS]

7. 7.

Yang, Y.-C.; Wang, H.-J.; Whang, J.; Huang, J.-S.; Lyu, L.-M.; Lin, P.-H.; Gwo, S.; Huang, M. H. Facet-Dependent Optical Properties of Polyhedral Au–Cu_2O Core–Shell Nanocrystals *Nanoscale* **2014**, 6, 4316–4324 DOI: 10.1039/c3nr06293g

[Crossref], [PubMed], [CAS]

8. 8.

Hsu, S.-C.; Liu, S.-Y.; Wang, H.-J.; Huang, M. H. Facet-Dependent Surface Plasmon Resonance Properties of Au–Cu_2O Core–Shell Nanocubes, Octahedra, and Rhombic Dodecahedra *Small* **2015**, 11, 195– 201 DOI: 10.1002/smll.201401916

[Crossref], [PubMed], [CAS]

9. 9.

Huang, M. H.; Rej, S.; Chiu, C.-Y. Facet-Dependent Optical Properties Revealed through Investigation of Polyhedral Au–Cu_2O and Bimetallic Core–Shell Nanocrystals *Small* **2015**, 11, 2716– 2726 DOI: 10.1002/smll.201403542

[Crossref], [PubMed], [CAS]

10. 10.

Rej, S.; Wang, H.-J.; Huang, M.-X.; Hsu, S.-C.; Tan, C.-S.; Lin, F.-C.; Huang, J.-S.; Huang, M. H. Facet-Dependent Optical Properties of Pd–Cu_2O Core–Shell Nanocubes and Octahedra *Nanoscale* **2015**, 7,11135– 11141 DOI: 10.1039/C5NR01411E

[Crossref], [PubMed], [CAS]

11. 11.

Wang, H.-J.; Yang, K.-H.; Hsu, S.-C.; Huang, M. H. Photothermal Effects from Au–Cu_2O Core–Shell Nanocubes, Octahedra, and Nanobars with Broad Near-Infrared Absorption Tunability *Nanoscale* **2016**, 8,965– 972 DOI: 10.1039/C5NR06847A

[Crossref], [PubMed], [CAS]

12. 12.

Warner, J. H.; Cao, H. Shape Control of PbS Nanocrystals Using Multiple Surfactants *Nanotechnology***2008**, 19, 305605 DOI: 10.1088/0957-4484/19/30/305605

[Crossref], [PubMed], [CAS]

13. 13.

Li, H.; Chen, D.; Li, L.; Tang, F.; Zhang, L.; Ren, J. Size- and Shape-Controlled Synthesis of PbSe and PbS Nanocrystals *via* a Facile Method *CrystEngComm* **2010**, 12, 1127– 1133 DOI: 10.1039/B917833C

[Crossref], [CAS]

14. 14.

Zhao, Z.; Zhang, K.; Zhang, J.; Yang, K.; He, C.; Dong, F.; Yang, B. Synthesis of Size and Shape Controlled PbS Nanocrystals and Their Self-Assembly *Colloids Surf., A* **2010**, 355, 114– 120 DOI: 10.1016/j.colsurfa.2009.12.009

[Crossref], [CAS]

15. 15.

Bakshi, M. S.; Thakur, P.; Sachar, S.; Kaur, G.; Banipal, T. S.; Possmayer, F.; Petersen, N. O. Aqueous Phase Surfactant Selective Shape Controlled Synthesis of Lead Sulfide Nanocrystals *J. Phys. Chem. C***2007**, 111, 18087– 18098 DOI: 10.1021/jp075477c

[ACS Full Text], [CAS]

16. 16.

Zhou, G.; Lü, M.; Xiu, Z.; Wang, S.; Zhang, H.; Zhou, Y.; Wang, S. Controlled Synthesis of High-Quality PbS Star-Shaped Dendrites, Multipods, Truncated Nanocubes, and Nanocubes and Their Shape Evolution Process *J. Phys. Chem. B* **2006**, 110, 6543– 6548 DOI: 10.1021/jp0549881

[ACS Full Text], [CAS]

17. 17.

Wang, Y.; Tang, A.; Li, K.; Yang, C.; Wang, M.; Ye, H.; Hou, Y.; Teng, F. Shape-Controlled Synthesis of PbS Nanocrystals via a Simple One-Step Process *Langmuir* **2012**, 28, 16436– 16443 DOI: 10.1021/la303738u

[ACS Full Text], [CAS]

18. 18.

Wu, J.-K.; Lyu, L.-M.; Liao, C.-W.; Wang, Y.-N.; Huang, M. H. Fast Synthesis of PbS Nanocrystals in Aqueous Solution with Shape Evolution from Cubic to Octahedral Structures and Their Assembled Structures *Chem. - Eur. J.* **2012**, 18, 14473– 14478 DOI: 10.1002/chem.201201687

[Crossref], [PubMed], [CAS]

19. 19.

Chen, H.-S.; Wu, S.-C.; Huang, M. H. Direct Synthesis of Size-Tunable PbS Nanocubes and Octahedra and the pH Effect on Crystal Shape Control *Dalton Trans.* **2015**, 44, 15088– 15094 DOI: 10.1039/C4DT03345K

[Crossref], [PubMed], [CAS]

20. 20.

Hohenberg, P.; Kohn, W. Inhomogeneous Electron Gas *Phys. Rev.* **1964**, 136, B864 DOI: 10.1103/PhysRev.136.B864

[Crossref]

21. 21.

Perdew, J. P.; Burke, K.; Ernzerhof, M. Generalized Gradient Approximation Made Simple *Phys. Rev. Lett.***1996**, 77, 3865– 3868 DOI: 10.1103/PhysRevLett.77.3865

[Crossref], [PubMed], [CAS]

22. 22.

Lyu, L.-M.; Wang, W.-C.; Huang, M. H. Synthesis of Ag_2O Nanocrystals with Systematic Shape Evolution from Cubic to Hexapod Structures and Their Surface Properties *Chem. - Eur. J.* **2010**, 16, 14167– 14174DOI: 10.1002/chem.201000563

[Crossref], [PubMed], [CAS]

23. 23.

Lyu, L.-M.; Huang, M. H. Formation of Ag_2S Cages from Polyhedral Ag_2O Nanocrystals and Their Electrochemical Properties *Chem. - Asian J.* **2013**, 8, 1847– 1853 DOI: 10.1002/asia.201300066

[Crossref], [PubMed], [CAS]

24. 24.

Wang, G.; Ma, X.; Huang, B.; Cheng, H.; Wang, Z.; Zhan, J.; Qin, X.; Zhang, X.; Dai, Y. Control led Synthesis of Ag_2O Microcrystals with Facet-Dependent Photocatalytic Activities *J. Mater. Chem.* **2012**, 22, 21189–21194 DOI: 10.1039/c2jm35010f

[Crossref], [CAS]

25. 25.

Kim, M.-J.; Cho, Y.-S.; Park, S.-H.; Huh, Y.-D. Facile Synthesis and Fine Morphological Tuning of Ag_2O*Cryst. Growth Des.* **2012**, 12, 4180– 4185 DOI: 10.1021/cg300681b

[ACS Full Text], [CAS]

26. 26.

Liu, S.-Y.; Shen, Y.-T.; Chiu, C.-Y.; Rej, S.; Lin, P.-H.; Tsao, Y.-C.; Huang, M. H. Direct Synthesis of Palladium Nanocrystals in Aqueous Solution with Systematic Shape Evolution *Langmuir* **2015**, 31, 6538–6545 DOI: 10.1021/acs.langmuir.5b01337

[ACS Full Text], [CAS]

27. 27.

Luth, H. *Solid Surfaces, Interfaces, and Films*; Springer-Verlag: Berlin, **2001**; p 408.

[Crossref]

28. 28.

Kulis, P.; Butikova, J.; Polyakov, B.; Marcins, G.; Pervenecka, J.; Pudzs, K.; Tale, I. Work Function of Colloidal Semiconducting Nanocrystals Measured by Kelvin Probe *IOP Conf. Ser.: Mater. Sci. Eng.* **2012**,38, 012048 DOI: 10.1088/1757-899X/38/1/012048

[Crossref], [CAS]

29. 29.

Nanda, K. K.; Sahu, S. N. Self-Assembled heterojunction between Electrodeposited PbS Nanoparticles and Indium Tin Oxide Substrate *Appl. Phys. Lett.* **2001**, 79, 2743– 2745 DOI: 10.1063/1.1413223

[Crossref], [CAS]

30. 30.

Nagpal, P.; Klimov, V. I. Role of Mid-Gap States in Charge Transport and Photoconductivity in Semiconductor Nanocrystal Films *Nat. Commun.* **2011**, 2, 486– 492 DOI: 10.1038/ncomms1492

[Crossref], [PubMed], [CAS]

31. 31.

Ip, A. H.; Thon, S.
M.; Hoogland, S.; Voznyy, O.; Zhitomirsky, D.; Debnath, R.; Levina, L.; Rollny, L. R.;Carey, G. H.; Fischer, A.; Kemp, K. W.; Kramer, I. J.; Ning, Z.; Labelle, A. J.; Chou, K.
W.; Amassian, A.;Sargent, E. H. Hybrid Passivated Colloidal Quantum Dot Solids *Nat. Nanotechnol.* **2012**, 7, 577– 582 DOI: 10.1038/nnano.2012.127

[Crossref], [PubMed], [CAS]

32. 32.

Kim, D.; Kim, D.-H.; Lee, J.-H.; Grossman, J. C. Impact of Stoichiometry on the Electronic Structure of PbS Quantum Dots *Phys. Rev. Lett.* **2013**, 110, 196802 DOI: 10.1103/PhysRevLett.110.196802

[Crossref], [PubMed], [CAS]

33. 33.

Luther, J. M.; Pietryga, J. M. Stoichiometry Control in Quantum Dots: A Viable Analog to Impurity Doping of Bulk Materials *ACS Nano* **2013**, 7, 1845– 1849 DOI: 10.1021/nn401100n

[ACS Full Text], [CAS]